Hydrology and Earth System Sciences

Estimating evaporation with thermal UAV data and two-source energy balance models

H. Hoffmann[1], H. Nieto[1], R. Jensen[1], R. Guzinski[1,a], P. Zarco-Tejada[2], and T. Friborg[1]

[1]Department of Geosciences and Natural Resource Management, University of Copenhagen, Øster Voldgade 10, 1350 Copenhagen, Denmark
[2]Instituto de Agricultura Sostenible (IAS), Consejo Superior de Investigaciones Científicas (CSIC), Campus Alameda del Obispo, Av. Menéndez Pidal s/n, 14004 Córdoba, Spain
[a]now at: DHI GRAS, Agern Allé 5, 2970 Hørsholm, Denmark

Correspondence to: H. Hoffmann (helene.hoffmann@ign.ku.dk)

Abstract. Estimating evaporation is important when managing water resources and cultivating crops. Evaporation can be estimated using land surface heat flux models and remotely sensed land surface temperatures (LST), which have recently become obtainable in very high resolution using lightweight thermal cameras and Unmanned Aerial Vehicles (UAVs). In this study a thermal camera was mounted on a UAV and applied into the field of heat fluxes and hydrology by concatenating thermal images into mosaics of LST and using these as input for the two-source energy balance (TSEB) modelling scheme. Thermal images are obtained with a fixed-wing UAV overflying a barley field in western Denmark during the growing season of 2014 and a spatial resolution of 0.20 m is obtained in final LST mosaics. Two models are used: the original TSEB model (TSEB-PT) and a dual-temperature-difference (DTD) model. In contrast to the TSEB-PT model, the DTD model accounts for the bias that is likely present in remotely sensed LST. TSEB-PT and DTD have already been well tested, however only during sunny weather conditions and with satellite images serving as thermal input. The aim of this study is to assess whether a lightweight thermal camera mounted on a UAV is able to provide data of sufficient quality to constitute as model input and thus attain accurate and high spatial and temporal resolution surface energy heat fluxes, with special focus on latent heat flux (evaporation). Furthermore, this study evaluates the performance of the TSEB scheme during cloudy and overcast weather conditions, which is feasible due to the low data retrieval alti-
tude (due to low UAV flying altitude) compared to satellite thermal data that are only available during clear-sky conditions. TSEB-PT and DTD fluxes are compared and validated against eddy covariance measurements and the comparison shows that both TSEB-PT and DTD simulations are in good agreement with eddy covariance measurements, with DTD obtaining the best results. The DTD model provides results comparable to studies estimating evaporation with similar experimental setups, but with LST retrieved from satellites instead of a UAV. Further, systematic irrigation patterns on the barley field provide confidence in the veracity of the spatially distributed evaporation revealed by model output maps. Lastly, this study outlines and discusses the thermal UAV image processing that results in mosaics suited for model input. This study shows that the UAV platform and the lightweight thermal camera provide high spatial and temporal resolution data valid for model input and for other potential applications requiring high-resolution and consistent LST.

1 Introduction

Evaporation (latent heat flux) serves as a key component in both hydrological and land–surface energy processes. However, it is often estimated indirectly because spatially distributed, physical measurements of evaporated water are cumbersome. Provided information on net solar radiation (R_n), sensible- (H), and soil heat flux (G), the latent heat

flux (LE) can be estimated as a residual using the assumption of surface energy balance in cases with no significant heat advection:

$$R_n = H + LE + G. \tag{1}$$

All terms in the above equation are related to the land surface temperature (LST). Since the 1980s, estimates of evaporation have been obtained through remotely sensed LST, and advanced land surface heat flux models accounting for vegetation, soil, and atmospheric conditions (Anderson et al., 1997; Kalma et al., 2008), and a large number of heat flux models exist with significant variations in physical system conceptualisation and input requirements (Boulet et al., 2012; Kustas and Norman, 1996; Stisen et al., 2008). Norman et al. (1995) applied the two-source energy balance model (TSEB) (Shuttleworth and Wallace, 1985) to remotely sensed data and this modelling scheme has proven to estimate reliable surface heat fluxes over cropland, rangeland, and forest at various spatial scales (Anderson et al., 2004; Norman et al., 2003). The TSEB modelling scheme generates robust estimates of surface heat fluxes despite being a simple solution scheme demanding relatively few input data. It was developed to be operational using thermal satellite images (Anderson et al., 2011), which serves as a key boundary condition in simulations. The TSEB modelling scheme partitions the remotely sensed LST into two layers; a canopy temperature and a soil temperature, using the Priestley–Taylor approximation (Norman et al., 2000). This enables a partition of heat flux estimations into its components from canopy and soil respectively. This approach is hereafter referred to as TSEB-PT in order to differentiate it from other TSEB approaches, such as TSEB-LUE (Houborg et al., 2012), based on the Light Use Efficiency concept, or TSEB-2ART, which utilises dual-angle LST observations for direct retrieval of soil and canopy temperatures (Guzinski et al., 2015).

Remotely sensed LST may deviate from the actual surface temperature by several degrees Kelvin due to atmospheric and surface emissivity effects. Consequently, thermal-based models utilising remotely sensed LST that do not address this issue are prone to producing less accurate results. Trying to overcome this issue, Norman et al. (2000) developed the dual-temperature-difference (DTD) model by incorporating two temperature observations into the TSEB modelling scheme: one conducted an hour after sunrise and another conducted later the same day when flux estimations are desired. One hour after sunrise, the surface heat fluxes are neglectable and observations acquired at this time represent a "starting point" for the temperatures collected later the same day. For agricultural and some hydrological purposes, there is a shortcoming in spatial and temporal resolution of satellite observations (Guzinski et al., 2014). This is especially true in areas where overcast weather conditions often occur, such as in northern Europe where the present study is conducted, as satellite thermal infrared and visible observations cannot penetrate clouds (Guzinski et al., 2013). Unmanned

aerial vehicles (UAVs) (or the Remotely Piloted Aircraft System, RPAS, in its most recent terminology) enable a critical improvement for spatial and temporal resolution of remotely sensed data. UAVs can operate at any specific time of day and year provided that strong wind and rainfall are absent. The relatively low flying height enables both data collection during overcast conditions (Hunt Jr. et al., 2005) and data with higher spatial resolution than what can be obtained by satellite. Here we hypothesise that UAV data can substitute satellite images and, in combination with the presented heat flux models, can be used to generate spatially detailed heat flux maps that provide insight into different evaporation rates and plant stress at decimetre scale. There is a rapidly growing interest in the potential of data collection with UAVs, particularly in the science of precision agriculture but also in a range of different scientific and commercial communities (Díaz-Varela et al., 2015; Gonzalez-Dugo et al., 2014; Swain et al., 2010; Zarco-Tejada et al., 2013, 2014). As scientists strive to understand the potential of UAVs and the new applications to which they are suited, the development of efficient workflows, operational systems, and improved software that capture and process UAV data are continuing (Harwin and Lucieer, 2012; Lucieer et al., 2014; Turner et al., 2012; Wallace et al., 2012). However, research into the possibilities and limitations of UAV platforms is still at an early stage and the present paper introduces the usage of UAV platforms into the fields of heat fluxes and hydrology.

In this study, surface energy balance components are estimated using LST retrieved with a UAV and used as input for the physically based TSEB models TSEB-PT and DTD. The aim is to assess whether a lightweight thermal camera installed on board a UAV is able to provide data of sufficient quality to attain high spatial and temporal resolution surface energy heat fluxes. Besides facilitating high-resolution LST, the UAV platform enables the application of TSEB-PT and DTD models in cloudy and overcast weather conditions. Model outputs are quantitatively validated with data from an eddy covariance system located at the same barley field over which the UAV flights were conducted and known irrigation patterns provide confidence to the spatially distributed evaporation variations revealed within the barley field. Additionally, this study outlines thermal UAV image processing which results in mosaics suited for model input.

1.1 Site

The TSEB models are applied in the HOBE (Hydrological OBsErvatory) agricultural site within the Skjern River catchment, western Denmark (see Fig. 1). The $400 \times 400\,\mathrm{m}$ site is located in the maritime climate zone where mild winters and cold summers result in a mean annual temperature of $8.2\,^{\circ}\mathrm{C}$ and a mean annual precipitation of $990\,\mathrm{mm}$. The prevailing winds are westerly and windy conditions are common; with $30\,\%$ of wind in 2014 coming from the westerly direction and an average wind speed of $3.8\,\mathrm{ms^{-1}}$. Cloudy and overcast

Table 1. UAV retrievals of LST, constituting 12 sets of input data to TSEB-PT and DTD. Early morning flights conducted 1 h after sunrise are only used in DTD; (c) means that data were collected during cloudy or overcast conditions.

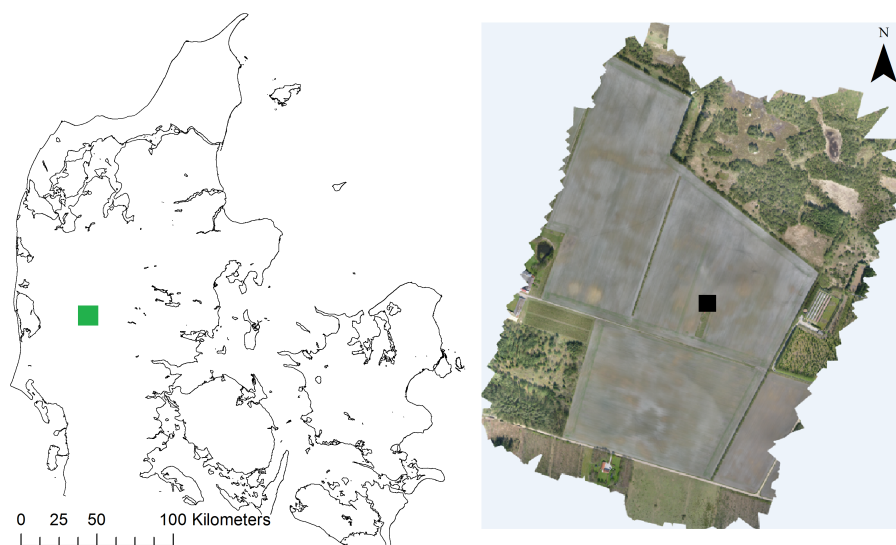| Date		Early flights $(T_{R,0(\theta)})$ Time (UTC)	Daylight flights $(T_{R,i(\theta)})$				
10 April 2014	(c)	07:00			11:30		
22 April 2014	(c)	06:00					14:30
15 May 2014		05:30			11:00	12:00	
22 May 2014	(c)	05:00	08:00	09:00	11:30	12:00	
18 June 2014	(c)	05:00			11:00	12:00	
2 July 2014	(c)	07:30			11:30		
22 July 2014		06:30				12:30	

Figure 1. HOBE agricultural site in western Denmark (56.037644° N, 9.159383° E). The black square represents the location of the eddy flux tower. The green square represents the location of the site.

weather conditions are frequent, with 1727 h of sunshine in 2014, which is 16 % above normal (Cappelen, 2015). The site was cultivated with barley during UAV campaigns. The soil profile consists of an upper 0.25 m plough layer of homogeneous sandy loam soil and a lower layer of course sand. Soil porosity of the upper and lower layer range between 0.35 and 0.40 and soil moisture content at field capacity is 26 %. The ability of the sandy material to retain water is limited and frequent irrigation is necessary to maintain crop growth during growing seasons (Ringgaard et al., 2011). The overall area is somewhat heterogeneous, consisting of three barley fields separated by a gravel road to the south and a row of conifers to the west. Conifers border the barley fields at several places. A meteorological tower with an eddy covariance system, consisting of a Gill R3-50 sonic anemometer and a LI-7500 open path infrared gas analyser, is located in the middle of the site (black square in Fig. 1). Meteorological

data used as input to the models and as heat flux validation are measured at this tower.

1.2 UAV campaign

UAV data were collected on 7 days distributed evenly during spring and summer 2014 (Table 1). In total 19 flights were conducted, of which 7 were flown early in the morning, constituting the additional input data for the DTD model. The entire airborne campaign thus resulted in 12 sets of input data for the TSEB-PT and DTD models. Dates with (c) in Table 1 mark days where the UAV flights were conducted in cloudy or overcast conditions.

A fixed-wing UAV (Q300, QuestUAV, UK) with a wingspan of 2.2 m was used as platform for the airborne operations. It was able to carry a payload of 2 kg for approximately 25 min in the air. With a speed of 60 km h^{-1} and flying height of 90 m above ground, the 400 × 400 m site area

was covered in a single flight. The UAV was controlled by the SkyCircuits Ltd SC2 autopilot in a dual redundant system with separate laptop and transmitter control. Communication between autopilot and ground was performed by a radio link that transmits position and attitude. Landing was conducted manually using the transmitter. SkyCircuits Ground Control Station software was used for generating the flight route and for visual inspection of the UAV, while it was in the air.

1.3   Thermal data and image processing

An Optris PI 450 LightWeight infrared camera of 380 g was mounted on the UAV. The camera detects infrared energy in the 7.5–13 μm thermal spectrum and surface temperatures were computed automatically using a fixed emissivity of unity. Thermal images were stored at 16 bit radiometric resolution. According to manufacturer specifications, the system has an accuracy of $\pm 2\,°C$ or $\pm 2\,\%$ at an ambient temperature of $23 \pm 5\,°C$. The thermal detector within the camera collects an image array of 382×288 pixels with a nadir viewing footprint of 50×40 m per image at 90 m flying height, resulting in an effective ground resolution of ~ 0.13 m per pixel.

Time synchronization between camera and autopilot was necessary in order to link the logged GPS and rotation position with each image. This was performed before launching the UAV with a USB GPS connected to the camera, thus synchronizing the timestamp on each image with the GPS clock. Timestamps were recorded in UTC time and were accurate to within 1 s. Re-calculation of camera position was therefore necessary and performed using a self-calibrating bundle adjustment in Agisoft PhotoScan software (Professional Edition version 1.0.4). No ground control points were used, nor needed, during camera alignment and bundle adjustment. Images were converted into unsigned 16 bit data to enable processing in PhotoScan.

Between 700 and 1000 images were collected for each flight with camera recording in continuous mode, triggering an image every second. Generally half of the images were suitable for further processing. Non-suitable images occur due to strong gusts of wind affecting flight velocity which causes poor-quality recording and blurry images. Images collected during take-off and landing were likewise discarded before post-processing. In addition to re-calculating the camera positions, the self-calibrating bundle adjustment computed three-dimensional point clouds from which thermal ortho-mosaics were built using a mean value composition. The view zenith angle of ortho-mosaics was set to 0° for all pixels, hence the largest possible amount of soil was assumed visible.

The thermal mosaics served as key boundary conditions to TSEB-PT and DTD. The resulting resolution on thermal mosaics from midday flights was 0.20 m. However, the software was not able to mosaic the early morning data, presumably because temperatures were too homogeneous to enable the detection of common features between images needed for

the bundle adjustment. Consequently, LST from early morning flights were extracted manually and only the average LST for the barley fields was used as the additional data input for DTD model runs. This average was a satisfying representation of early morning LST because of its homogeneous nature.

1.4   Heat flux models

The original TSEB model developed by Norman et al. (1995) is a two-layer model of turbulent heat exchange. Observations of remotely sensed LST are split into two layers: a canopy (T_C) and a soil (T_S) temperature. This is performed with the Priestley–Taylor approximation that enables calculations of canopy sensible heat flux using estimates of net radiation divergence. The initial estimate of canopy sensible heat flux thus permits separation of sensible and latent heat flux between canopy and soil. Further, it eliminates the need for an empirical excess resistance term (Monteith, 1965), which addresses a substitution of directional radiometric temperature with aerodynamic temperature when calculating sensible heat fluxes (Eqs. 5, 8, and 9 in Norman et al., 1995). The TSEB modelling scheme uses directional radiometric temperature (collected with the thermal camera and UAV) and therefore no substitution of temperatures or correction via the excess resistance is needed. Sections 1.4.1 and 1.4.2 contain TSEB equations of relevance for the present study and highlight the difference between TSEB-PT and DTD computations.

1.4.1   TSEB-PT

Net radiation (R_n) and the three resistances in this soil–canopy–atmosphere heat flux network – the aerodynamic resistance to heat transfer (R_A), the resistance to heat transport from soil surface (R_S), and the total boundary layer resistance of leaf canopy (R_X) (all in s m^{-1}) – remain constant during the individual model runs. For calculations of R_A and R_S, see Norman et al. (2000), Eqs. (10) and (11); for calculations on R_X see Norman et al. (1995), Eq. (A8). R_n is calculated as a sum of short- and long-wave radiation:

$$R_n = \left(R_{s,in} - R_{s,out}\right) + \left(R_{l,in} - R_{l,out}\right) \tag{2}$$

$$R_{s,in} - R_{s,out} = R_{s,in}(1 - \alpha) \tag{3}$$

$$R_{l,in} - R_{l,out} = \epsilon_{surf}\epsilon_{atm}\sigma T_A^4 - \epsilon_{surf}\sigma T(\theta)_R^4, \tag{4}$$

where R_s, R_l is short- and long-wave radiation respectively, subscripts "in" and "out" refer to the direction of the radiation, α is the combined vegetation and soil albedo, σ is the Stefan–Boltzman constant, T_A is air temperature (K), $T(\theta)_R$ is radiometric land surface temperature (K), ϵ_{surf} is combined vegetation and soil emissivity, and ϵ_{atm} is atmosphere emissivity. The α was estimated from incoming and outgoing short-wave radiation from a four-component radiation sensor (NR01, Hukseflux Thermal Sensor). Albedo for

bare soil was measured before the first barley shoots appeared on the surface and was kept fixed (although some changes are expected with soil humidity) whereas albedo for vegetation was retrieved for each flying day and hence varied between individual model runs. Combined vegetation and soil albedo for each flying day is shown in Table 2. T_A was attained from the meteorological tower (Sect. 1.1) and $T(\theta)_R$ was collected with the UAV. ϵ_{surf} was obtained under similar conditions as in Guzinski et al. (2014) and ϵ_{atm} was computed as in Brutsaert (1975):

$$\epsilon_{atm} = 1.24 \left(\frac{e_a}{T_A} \right)^{0.14286} \quad (5)$$

where e_a is water vapour pressure (mb) attained from the meteorological tower.

Assuming neutral atmospheric stability and the Monin–Obukhov length tending to infinity, the iterative part of the model is then initiated.

During the first iteration the net radiation divergence, partitioning R_n into radiation reaching the soil ($R_{n,S}$) and the canopy ($R_{n,C}$) respectively, is computed as in Norman et al. (2000):

$$\Delta R_n = R_n \left[1 - \exp \left(\frac{-\kappa F \Omega_0}{\sqrt{2 \cos(\theta_s)}} \right) \right], \quad (6)$$

where Ω_0 is the nadir view clumping factor that depends on the ratio of vegetation height to plant crown width which is set to 1.0, θ_s is the sun zenith angle calculated by model from time of the day, κ is an extinction coefficient varying smoothly from 0.45 for LAI more than 2 to 0.8 for LAI less than 2, and F is the total Leaf Area Index (LAI). Measurements of LAI were obtained with a canopy analyser LAI2000 instrument three times during the UAV campaign: on 21 May 2014, 3 June 2014, and 18 June 2014. A LAI average from six measurement locations in the barley site was computed for each of the three dates: 3.9, 6.6, and 4.0 respectively. LAI values for each model run were extrapolated from the measurements taking canopy height and fraction of green vegetation into account.

Sensible heat flux of the canopy can thus be estimated using the Priestley–Taylor approximation:

$$H_C = \Delta R_n \left(1 - \alpha_{PT} f_g \frac{sp}{sp + \gamma} \right) \quad (7)$$

where α_{PT} is the Priestley–Taylor parameter set to an initial value of 1.26 assuming unstressed vegetation transpiration (Priestley and Taylor, 1972), f_g is fraction of vegetation that is green which was estimated in situ for each flying day (Table 2), sp is the slope of saturation pressure curve, and γ is the psychometric constant, both obtained from Allen et al. (1998).

Using the sensible heat flux from canopy, canopy temperature (T_C) can be computed using Eqs. (A7), (A11), (A12),

Table 2. Changing input parameters for each flying day.

Date	LAI	Canopy height (m)	Green veg. fraction	Albedo$_{soil+veg.}$
10 April 2014	0.48	0.02	1	0.142
22 April 2014	0.88	0.08	1	0.181
15 May 2014	1.49	0.12	1	0.182
22 May 2014	3.90	0.30	1	0.226
18 June 2014	4.03	0.95	0.7	0.181
2 July 2014	3.43	1.10	0.3	0.202
22 July 2014	3.02	1.20	0.02	0.189

and (A13) from Norman et al. (1995). Calculations of soil temperature (T_S) can thus be performed:

$$T_S = \left(\frac{T(\theta)_R^4 - f_\theta T_C^4}{1 - f_\theta} \right)^{0.25}, \quad (8)$$

where f_θ is fraction of view of radiometer covered by vegetation calculated as $f_\theta = 1 - \exp(\frac{-0.5\Omega_\theta F}{\cos(\theta)})$, where Ω_θ is the clumping factor at view zenith angle (θ).

With known resistances and temperatures, fluxes are then calculated in the following sequence (all in W m^{-2}):

$$H_C = \rho c_p \frac{T_C - T_{AC}}{R_X}, \quad (9)$$

where H_C is sensible heat flux from canopy, ρ is air density (kg m^{-3}), c_p is specific heat of air (J kg^{-1} K^{-1}), and T_{AC} is inter-canopy air temperature (K) computed with T_A, T_S, T_C, and resistances.

Canopy latent heat flux is computed as

$$LE_C = \Delta R_n - H_C. \quad (10)$$

Sensible heat flux from soil is computed as

$$H_S = \rho c_p \frac{T_S - T_{AC}}{R_S}. \quad (11)$$

Soil heat flux is computed following Liebethal and Foken (2007):

$$G = 0.3 R_{n,s} - 35, \quad (12)$$

where $R_{n,s}$ is net radiation that reaches the soil surface computed as $R_{n,S} = R_n - \Delta R_n$. Soil latent heat flux is computed as

$$LE_S = R_{n,s} - G - H_S. \quad (13)$$

Now it is possible to calculate the total sensible- (H) and latent heat fluxes (LE) as a summation of their canopy and soil components: $H = H_C + H_S$ and $LE = LE_C + LE_S$.

The Monin–Obukhov length is then re-calculated according to Eq. (2.46) of Brutsaert (2005), and the iterative part of the model is re-run until the Monin–Obukhov length converges to a stable value, at which point the final flux values are attained.

1.4.2 DTD

The DTD model described in Norman et al. (2000) is a further development of the TSEB-PT model. DTD similarly splits the observed LST into canopy and soil temperatures and computes surface energy balance components following virtually the same procedure. However, DTD accounts for the discrepancy between the fact that the TSEB modelling scheme is sensitive to the temperature difference between land surface and air, and that absolute LST retrieved from remote sensing data are regarded as inaccurate. This is accounted for by adding an additional input data set: LST retrieved 1 h after sunrise when energy fluxes are minimal. The modelled fluxes are hence based on a temperature difference between the two observations, which is assumed to be a more robust parameter compared to a single retrieval of remotely sensed LST as it minimizes consistent bias in the temperature estimates. The essential equation that differs between TSEB-PT and DTD is the one computing sensible heat flux. In the series implementation of DTD the linear approximation of Eq. (8) is taken together with Eqs. (9) to (11) and applied at midday and 1 h after sunrise, which values are subsequently subtracted from each other to arrive at the following:

$$
H_i = \rho c_p \left[\frac{\left(T_{R,i}\left(\theta_i\right) - T_{R,0}\left(\theta_0\right)\right) - \left(T_{A,i} - T_{A,0}\right)}{(1 - f\left(\theta_i\right)) R_{S,i} + R_{A,i}} \right]
$$
$$
+ H_{C,i} \left[\frac{(1 - f\left(\theta_i\right)) R_{S,i} - f\left(\theta_i\right) R_{X,i}}{(1 - f\left(\theta_i\right)) R_{S,i} + R_{A,i}} \right], \tag{14}
$$

where subscripts i and 0 refer to observations at midday and 1 h after sunrise respectively. Since the early morning (time 0) sensible heat fluxes are negligible they are omitted in the above equation.

Computations of soil heat flux (G) also differ because the difference in radiometric temperature between early morning and midday observations can be used as an approximation of the diurnal variation in soil surface temperature. Soil heat flux computations are derived from the soil heat flux model of Santanello and Friedl (2003):

$$
G = R_{n,S} A \cos \left(2\pi \frac{t + 10\,800}{B} \right) \tag{15}
$$

where t is time in seconds between the observation time and solar noon, $A = 0.0074 \Delta T_R + 0.088$, $B = 1729 \Delta T_R + 65\,013$, and ΔT_R is an approximation of the diurnal variation in the soil surface temperature from UAV data.

For an in-depth review of the TSEB-PT and DTD models including all equations, see Guzinski et al. (2014, 2015).

1.5 Footprint extraction from model output maps

In order to compare modelled R_n, H, G, and LE to measurements from the eddy covariance system, a single representative value from each TSEB-PT and DTD output map has to be extracted in accordance with the coverage of the eddy covariance footprints. Each eddy flux measurement represents an area for which the size, shape, and location are determined by surface roughness, atmospheric thermal stability, and wind direction at a given time – in this case UAV flight times. Sensible and latent heat fluxes are extracted from TSEB-PT and DTD maps using a two-dimensional footprint analysis approach as described in Detto et al. (2006). The 12 footprint outputs were applied to corresponding maps of sensible and latent heat fluxes by weighing each modelled pixel according to the contribution of that pixel's location to the measured flux. Approximations of the 70 % eddy flux footprint coverages are shown in Appendix B. Net radiation and soil heat flux measurements have footprints that are much smaller than sensible and latent heat flux measurements and values from R_n and G output maps were extracted from a 5×5 m area on the barley field next to the eddy flux tower.

1.6 Validation data

The eddy covariance system consisting of a Gill R3-50 sonic anemometer and a LI-7500 open path infrared gas analyser is located 6 m above ground in the middle of the site (see Fig. 1). Wind components in three dimensions and concentrations of water vapour were measured at 10 Hz. Sensible and latent heat fluxes for validation of model outputs were computed from the eddy covariance system using EddyPro 5.1.1 software (Fratini and Mauder, 2014). Computations include two-dimensional coordinate rotation, block averaging of measurements in 30 min windows, corrections for density fluctuations (Webb et al., 1980), spectral corrections (Moncrieff et al., 1997, 2005), and measurement quality checking according to Mauder and Foken (2006). Furthermore, the computed heat fluxes were subject to an outlier quality control following procedures described in Papale et al. (2006). Short- and long-wave, incoming, and outgoing radiation and soil heat fluxes were measured with a Hukseflux four-component net radiometer (model NR01) and heat flux plate (model HFP01). Gap-filling of the validation data was not required because no gaps in the data occurred during the 12 flights. When applying the surface energy balance expression any residual was assigned to latent heat flux, as recommended by Foken et al. (2011). This ensures energy balance closure and comparability with TSEB-PT and DTD modelled fluxes. The average size of residuals from the 12 data sets was 9 %.

2 Results and discussion

TSEB-PT and DTD models are executed 12 times with data collected on 7 days during the spring and summer of 2014. Spatially distributed maps of net radiation, soil-, sensible-, and latent heat fluxes are attained with resolutions of 0.20 m.

Table 3. Measured and modelled net radiation (R_n), sensible heat flux (H), latent heat flux (LE), and soil heat flux (G). Dates marked with (c) represent days with cloudy or overcast conditions.

Date, time (UTC)		Measured (W m^{-2})				TSEB-PT (W m^{-2})				DTD (W m^{-2})			
		R_n	H	LE	G	R_n	H	LE	G	R_n	H	LE	G
10 April 2014 11:30	(c)	243	87	105	50	155	15	134	2	155	20	121	8
22 April 2014 14:30	(c)	203	73	81	49	180	1	181	4	180	62	118	−2
15 May 2014 11:00		453	124	241	88	401	42	330	27	401	75	295	25
15 May 2014 12:00		619	132	385	102	600	49	492	54	600	97	472	26
22 May 2014 08:00	(c)	270	33	206	31	284	−20	296	2	284	95	179	−1
22 May 2014 09:00	(c)	306	−26	290	43	301	−48	337	10	301	63	231	1
22 May 2014 11:30	(c)	406	−16	367	55	397	−33	418	14	397	101	287	6
22 May 2014 12:00	(c)	440	14	365	61	436	−51	465	21	436	42	387	4
18 June 2014 11:00	(c)	538	158	326	55	505	89	397	27	505	191	309	9
18 June 2014 12:00	(c)	631	200	378	52	612	54	514	43	612	156	450	7
2 July 2014 11:30	(c)	217	54	152	11	121	−9	135	−8	121	52	68	1
22 July 2014 12:30		479	282	161	36	511	125	335	52	511	211	293	6

Table 4. Root mean square error (RMSE), mean absolute error (MAE) and correlation coefficient (r) computed for TSEB-PT and DTD results. Values in parentheses are RMSE and MAE respectively as percentage (%) of measured fluxes.

	TSEB-PT			DTD		
	RMSE (W m^{-2})	MAE (W m^{-2})	r	RMSE (W m^{-2})	MAE (W m^{-2})	r
R_n	44 (11)	33 (8)	0.98	44 (11)	33 (8)	0.98
G	38 (72)	35 (66)	0.58	48 (91)	45 (86)	0.86
H	85 (91)	75 (81)	0.96	59 (64)	49 (52)	0.74
LE	94 (37)	84 (33)	0.92	67 (26)	57 (22)	0.85

2.1 Comparison between UAV fluxes and fluxes from eddy covariance

Modelled fluxes attained with thermal UAV data and measured fluxes from the eddy covariance system are shown in Table 3. As expected, there are large variations throughout the season determined primarily by time of year and time of day – dates and hours with potentially large incoming solar radiation (summer and midday) contain the potential for largest evaporation. Figure 2a–c show modelled versus measured fluxes and a statistical comparison is presented in Table 4.

Calculations for R_n are alike in TSEB-PT and DTD and generally in good agreement with measured R_n with a RMSE value of 44 W m^{-2} (11 %) and a correlation coefficient (r) of 0.98 (Table 4). Simulated R_n from 10 April and 2 July 2014 are in less good agreement with measured R_n and are underestimated with 88 and 96 W m^{-2} respectively (Table 3).

Sensible heat fluxes (H) are well estimated by both models (Tables 3 and 4 and Fig. 2b). TSEB-PT sensible heat fluxes are consistently underestimated; however, the correlation coefficient (r) is better (in contrast to RMSE and MAE) than r calculated for DTD. This implies a better linear relation between measured and modelled sensible heat flux from TSEB-PT (see Fig. 2b). The DTD model computes slightly more scattered sensible heat fluxes but results do not show any systematic errors – they are centred around measured values and are generally in better accordance with measured fluxes with RMSE and MAE values of 59 W m^{-2} (64 %) and 49 W m^{-2} (52 %), compared to TSEB-PT RMSE and MAE values of 85 W m^{-2} (91 %) and 75 W m^{-2} (81 %).

Soil heat fluxes (G) are underestimated by both algorithms, and RMSE and MAE values of 48 W m^{-2} (91 %) and 45 W m^{-2} (86 %), and 38 W m^{-2} (72 %) and 35 W m^{-2} (66 %) are obtained from DTD and TSEB-PT, respectively.

Modelled latent heat flux (LE) is in good agreement with measured latent heat fluxes. As a consequence of underestimation of sensible heat flux in TSEB-PT simulations, a small overestimation of TSEB-PT latent heat flux appears (Fig. 2c). DTD latent heat flux is again more scattered but with lower RMSE and MAE values of 67 W m^{-2} (26 %) and 57 W m^{-2} (22 %), compared to TSEB-PT RMSE and MAE values of 94 W m^{-2} (37 %) and 84 W m^{-2} (33 %).
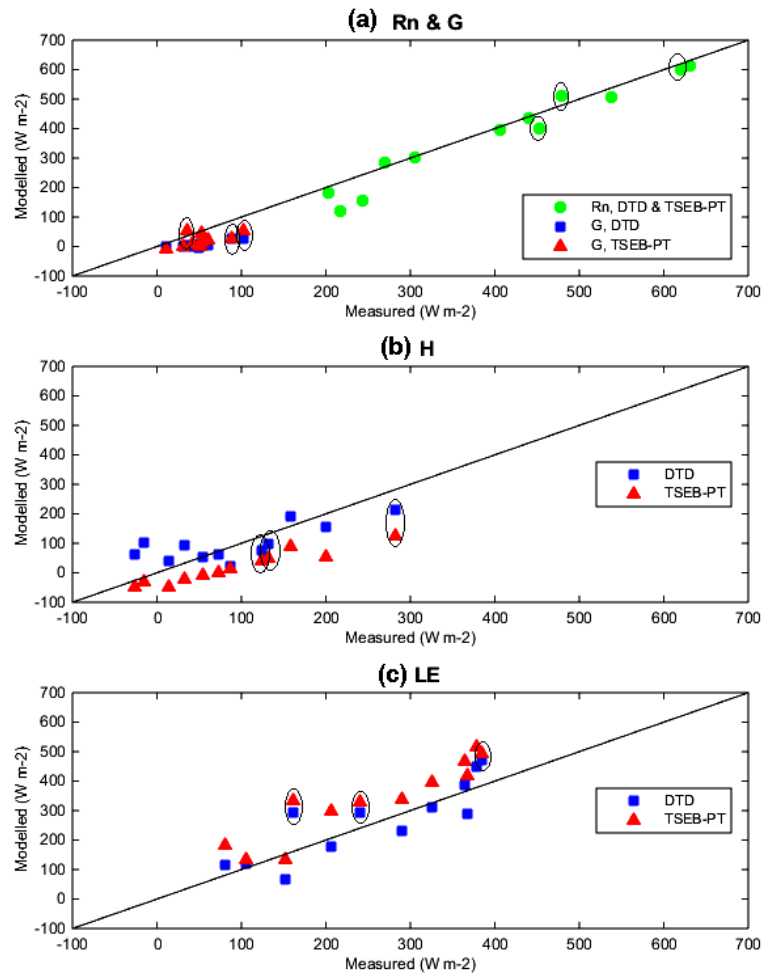
Figure 2. Modelled vs. measured net radiation (R_n), soil- (G), sensible- (H), and latent heat fluxes (LE). Data collected in sunny weather conditions are enclosed by black circles.

2.1.1 Method discussion

The DTD algorithm generally produces results in better accordance with measurements and is concluded to be a better algorithm when simulating heat fluxes with the present experimental setup. This suggests a consistent bias in the UAV-derived LST which can be corrected by subtracting the early morning observations from the midday ones, and demonstrates the robustness and added utility of the DTD approach.

A poor agreement between modelled and measured R_n was found on 10 April and 2 July 2014. Modelled R_n consists of short- and long-wave incoming and outgoing radiation ($R_{s,in}$, $R_{s,out}$, $R_{l,in}$, $R_{l,out}$) of which $R_{s,in}$ is provided as model input from eddy tower measurements. This contributes positively to the agreement between modelled and measured R_n but it cannot be assigned to model performance or the quality of collected LST data. Therefore a comparison is also conducted between modelled and measured net long-wave radiation (R_l) which, as opposed to modelled and measured R_n,

are entirely independent of each other. The TSEB modelling scheme produces R_l estimates to a satisfactory level if results from 10 April and 2 July are not regarded (see Appendix A). R_l estimates depend on atmospheric emissivity which in the TSEB modelling scheme are calculated with Eq. (5) (from Brutsaert, 1975). Equation (5) builds on the assumption of exponential atmospheric profiles for temperature, pressure, and humidity. The stability of atmosphere is affected by relative humidity (RH) (Herrero and Polo, 2012) and errors between measured and modelled R_l are related to RH in the second graph in Appendix A. A coincidence between the highest errors and the highest RH appears. This suggests that the assumptions behind Eq. (5) might not be met on 10 April and 2 July. Different approaches for estimating R_l could have been chosen for these two dates (e.g. Brutsaert, 1982) but for simplicity the approach presented in Brutsaert (1975) is maintained for all dates. Appendix A show that if algorithm assumptions are met, UAV-collected LST can be satisfactorily used to estimate R_l using the TSEB scheme. Equation (5)

also builds on the assumption of clear skies. Since poor simulation of R_l is not significant in data collected in overcast conditions, the larger incoming long-wave radiation due to clouds might compensate for the smaller path between UAV and surface, compared to between satellite and surface.

Further, a poor agreement between modelled and measured G was found. G was measured from two heat flux plates located approximately 3 cm below the surface. Heat flux plates might not provide the best estimate of energy partitioning at the surface (Jansen et al., 2011) which could lead to uncertainties in measured G. Further, the difference between heat conduction of soil and air create a discrepancy between measured G and H and LE, since fast changes in R_n (as a consequence of intermittent cloud cover) will have a faster response in H and LE than in G (Gentine et al., 2012). The TSEB modelling scheme does not account for the delay in G response and therefore also a discrepancy between measured and modelled G will occur. However, the magnitude of G is small compared to the remaining surface energy fluxes and therefore has a comparably small impact on LE estimations even though it is computed as a residual of R_n, H, and G.

On average there was a 95 % overlap between the coverage of eddy flux footprints and the model output maps from all 12 data sets. The missing percentages of fluxes from maps were simply added from the flux values obtained from overlapping eddy flux footprints and maps. This introduces a small uncertainty to the extraction of flux values from model output and thus also to the comparison between measured and modelled H and LE.

The view zenith angle of ortho-mosaics was set to 0° (Sect. 1.3). However, the maximum view zenith angle of the thermal camera is 15° and setting a theoretical view zenith angle to 0° could lead to a small overestimation of latent heat flux. Any bias due to the 0° view zenith angle in models could perhaps have been accommodated using a maximum value composition (instead of a mean value composition) when generating LST mosaics. However, a mean value composition was used because the mosaics produced with this method compared well with mosaics produced manually in which the edges of each image were removed. Edges were removed in order to eliminate the vignetting effect, which generally affects thermal images in particular and therefore also the images collected in this study. Using a mean value composition is thus assumed to enable the usage of entire images without eliminating or correcting for vignetting effects. Using entire images allows a larger image overlap which is crucial when images are mosaicked in Photoscan. The difference between using a mean and a maximum value composition was ∼ 0.3° Kelvin and 5 W m^{-2} latent heat flux for the mosaic from 10 April 2014.

Disagreement between measured and modelled fluxes may also be due to the presented approach of handling the residual between eddy covariance surface energy fluxes. The average size of residuals from the 12 data sets was as mentioned 9 %

(Sect. 1.6). A different approach to handling the energy balance residual (e.g. Foken, 2008) would lead to slightly different results in the comparison between measured and modelled fluxes.

A calibration of the camera with in situ temperatures would likely have improved TSEB-PT heat flux computations. Further, a conversion of brightness temperature to actual LST using a spatially distributed emissivity would presumably improve both TSEB-PT and DTD results.

2.1.2 Comparison to other studies

Guzinski et al. (2014) applied their TSEB-PT study to the same field site as the present study but they used thermal satellite images from Landsat as boundary conditions as opposed to thermal UAV images. A comparison between the two studies shows similar accurate results. Guzinski et al. (2014) achieve RMSEs of 46 W m^{-2} for R_n, 56 W m^{-2} for H, and 66 W m^{-2} for LE (Table 2, column ND$_H$ in Guzinski et al., 2014). This study achieves RMSEs of 44 W m^{-2} for R_n, 59 W m^{-2} for H and 67 W m^{-2} for LE, using the DTD model. The r is likewise similar between the two studies. However, when Guzinski et al. (2014) uses both MODIS and Landsat data to disaggregate DTD fluxes, modelled sensible and latent heat fluxes were in better agreement with the observed fluxes (Table 2, column EF in Guzinski et al., 2014). Further, a comparison between this study and other studies seeking to estimate surface fluxes from remotely sensed data (such as Colaizzi et al., 2012; Guzinski et al., 2013; Norman et al., 2000) shows that measured and modelled fluxes are of the same order of agreement.

2.1.3 Cloudy and overcast situation

Contrary to studies using satellite images, the majority of data in this study were retrieved under cloudy or overcast conditions. Data collected during sunny conditions are enclosed by black circles in Fig. 2a–c and Table 5 shows statistical parameters calculated using only data from days with cloudy or overcast weather conditions. Based on Fig. 2a–c and on a comparison between statistical parameters in Tables 4 and 5, no significant difference can be seen between data collected during cloudy, overcast and sunny weather conditions. Thus it is concluded that the TSEB modelling scheme can be applied to data obtained in all three weather types. However, it is worth mentioning that data collected during conditions with scattered clouds, and hence quickly changing irradiance, would lead to large variations in retrieved LST during a single flight. LST collected with UAVs are instantaneous but also a mosaic of instantaneous LST collected in a time span of 20 min. Comparing this kind of measurement to a 30 min flux average from the eddy covariance system can lead to disagreement between measured and modelled fluxes (Kustas et al., 2002).

Table 5. Statistical parameters based on data that were collected during only cloudy and overcast weather conditions (nine dates). Root mean square error (RMSE), mean absolute error (MAE), and correlation coefficient (r) computed for TSEB-PT and DTD results. Values in parentheses are RMSE and MAE respectively as percentage (%) of measured fluxes.

	TSEB-PT			DTD		
	RMSE (W m^{-2})	MAE (W m^{-2})	r	RMSE (W m^{-2})	MAE (W m^{-2})	r
R_n	40 (11)	32 (8)	0.99	40 (11)	32 (8)	0.99
G	30 (66)	33 (72)	0.66	38 (83)	42 (92)	0.61
H	63 (99)	64 (100)	0.84	53 (83)	50 (78)	0.69
LE	69 (27)	71 (28)	0.98	46 (18)	46 (18)	0.95

2.2 Spatial patterns in evaporation maps

Combining the high spatial resolution LST with the TSEB modelling scheme produces spatially distributed heat flux maps which reveal patterns in the evaporation which could not have been quantified through more established techniques, such as eddy covariance or when using satellite data. Twelve evaporation maps computed with DTD are shown in Appendix B. Patterns of evaporation within the barley fields are the same for TSEB-PT and DTD maps. The maps differ in size due to different flight routes, which are determined by wind direction and velocity on the given day. This study does not have access to data with the same spatial resolution that could have validated the evaporation patterns. However, the irrigation system applied to the barley field constitutes a valid explanation for the patterns seen in maps from the late growing season, which provides confidence in the spatial patterns seen in all maps.

During the UAV campaign the barley field was irrigated five times: 23 May, 29 May, 5 June, 15 June, and 25 June 2014. On each occasion 25 mm of water was applied. Irrigation is performed with a travelling irrigation gun that is automatically pulled across the field in tramlines that run in north–south direction in the northern field and the east–west direction in the southern field (Fig. 3). The pattern in which water is distributed remains the same during the entire growing season.

The evaporation maps from 18 June 2014 and onwards (when irrigation would plausibly have made its mark on plant health) reveal significant differences within the barley fields: patterns of ∼ 20 m wide blueish areas running parallel to the tramlines. The blueish colour illustrates that these areas produce less evaporation than surrounding areas. The location of areas with smaller evaporation rates corresponds well with areas where irrigation guns have not been able to irrigate as intensively as areas closer to the tramlines (Fig. 3). Areas furthest away from tramlines thus likely consist of less healthy plants which will generate higher LST and lower rates of evaporation. Recognition of very likely patterns of evaporation within the barley field demonstrates a high degree of
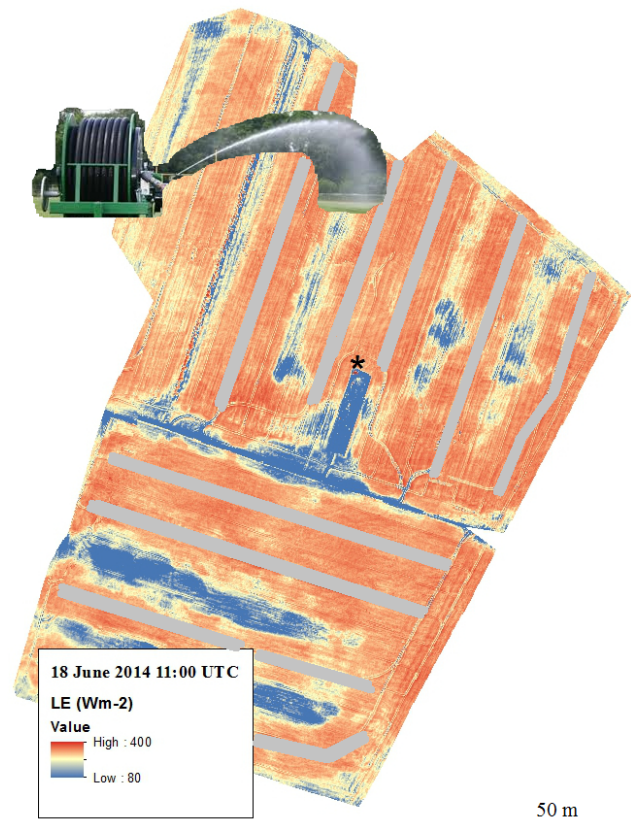

Figure 3. Grey lines highlight tramlines in which irrigation guns are placed at all five irrigation events in 2014. The underlying map shows evaporation patterns on 18 June 2014. Red colours are high evaporation and blue colours are low evaporation. Patterns of lower evaporation correspond well with areas being furthest away from irrigation guns.

confidence in the veracity of the spatially distributed model output.

3 Conclusions and outlook

Land surface temperatures (LST) were obtained with a lightweight thermal camera mounted on a UAV with the ability to cover a 400×400 m barley field in a single flight. Thermal images were successfully concatenated into high-resolution LST mosaics (0.2 m) that served as key boundary conditions to the two-source energy balance models: TSEB-PT and DTD. In contrast to TSEB-PT, the DTD model accounts for biases in remotely sensed LST, likely to be present in images from the lightweight thermal camera. Simulated net radiation, soil-, sensible-, and latent heat fluxes were generally in good agreement with flux measurements from an eddy covariance system, with the DTD algorithm showing superior results. Patterns from systematic irrigation on the barley field support the confidence in the veracity of the spatially distributed evaporation patterns produced by the models. A comparison between present results and results from other studies estimating surface energy fluxes from heat flux models and remotely sensed LST reveals that data from the UAV platform and the lightweight thermal camera generate surface energy fluxes with similar accuracy as can be generated using satellite data. The UAV data can thus be used for model input and for other potential applications requiring good quality, consistent, and high-resolution LST.

Additionally, the UAV platform accommodated validation of the applicability of the TSEB modelling scheme in cloudy and overcast weather conditions which was possible due to the low altitude of LST retrievals compared to satellites that can only retrieve LST during clear-sky conditions.

Future improvements will incorporate spatially distributed optical data into the TSEB models in order to estimate spatially varying ancillary variables such as albedo, leaf area index, and canopy height. This will enable flux estimations in areas with heterogeneous vegetation types and have a positive effect on estimations over maturing crops when differences in irrigation may have impacted their developmental stage. Extending the present setup to other land cover types would further strengthen the applicability of thermal UAV data and the presented model scheme.

A calibration of the thermal camera with in situ temperatures should improve TSEB-PT results with a potential positive effect on DTD results as well.

Adjustments in the TSEB modelling scheme that consider differences between satellite and UAV images might be valuable. The atmospheric path from the ground to satellites and from the ground to UAVs differs greatly and a comparison between measured and modelled long-wave radiation in this study (Sect. 2.1.1) reveals that a different approach for estimating atmospheric emissivity (when using UAV data) might further improve the TSEB modelling results.

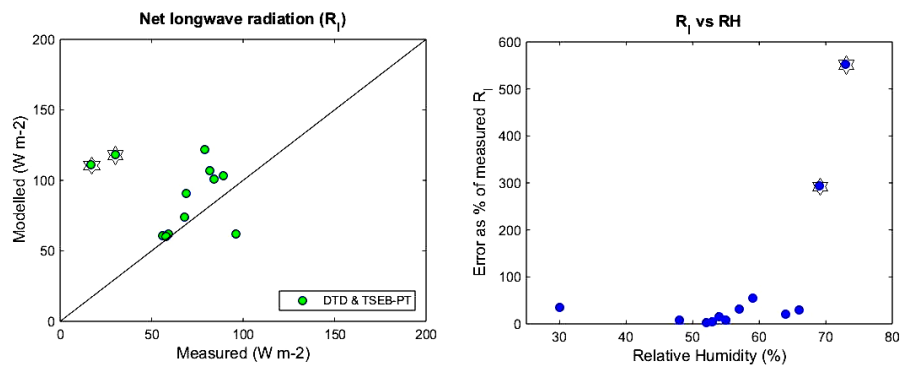## Appendix A: Net long-wave radiation

Figure A1. The first graph shows measured and modelled net long-wave radiation (R_l). R_l from 10 April and 2 July 2014 are enclosed by black stars. The second graph shows the error between measured and modelled R_l as a percentage of measured R_l compared to relative humidity at the time of UAV flights. Again, measurements from 10 April and 2 July 2014 are enclosed by black stars.
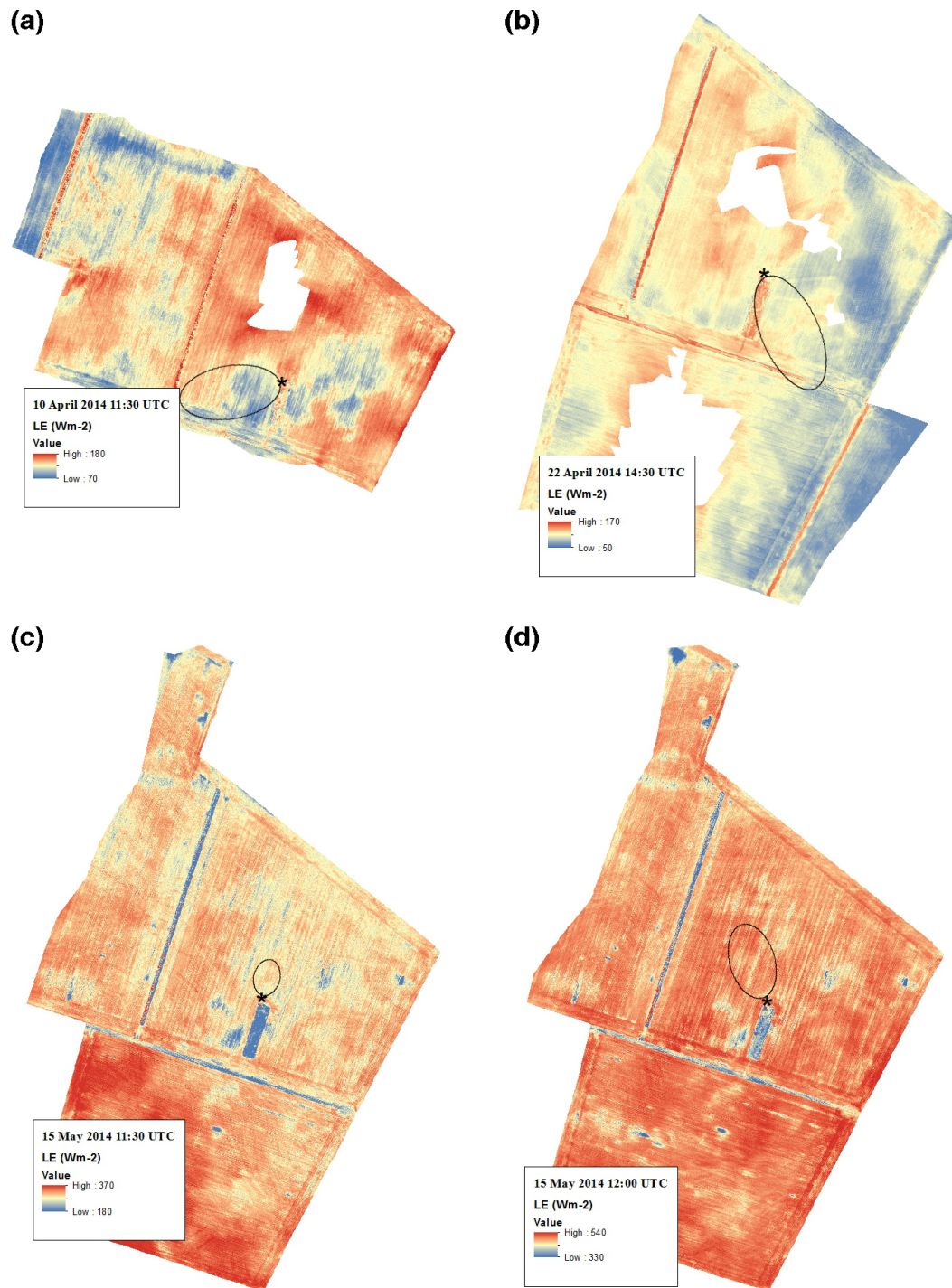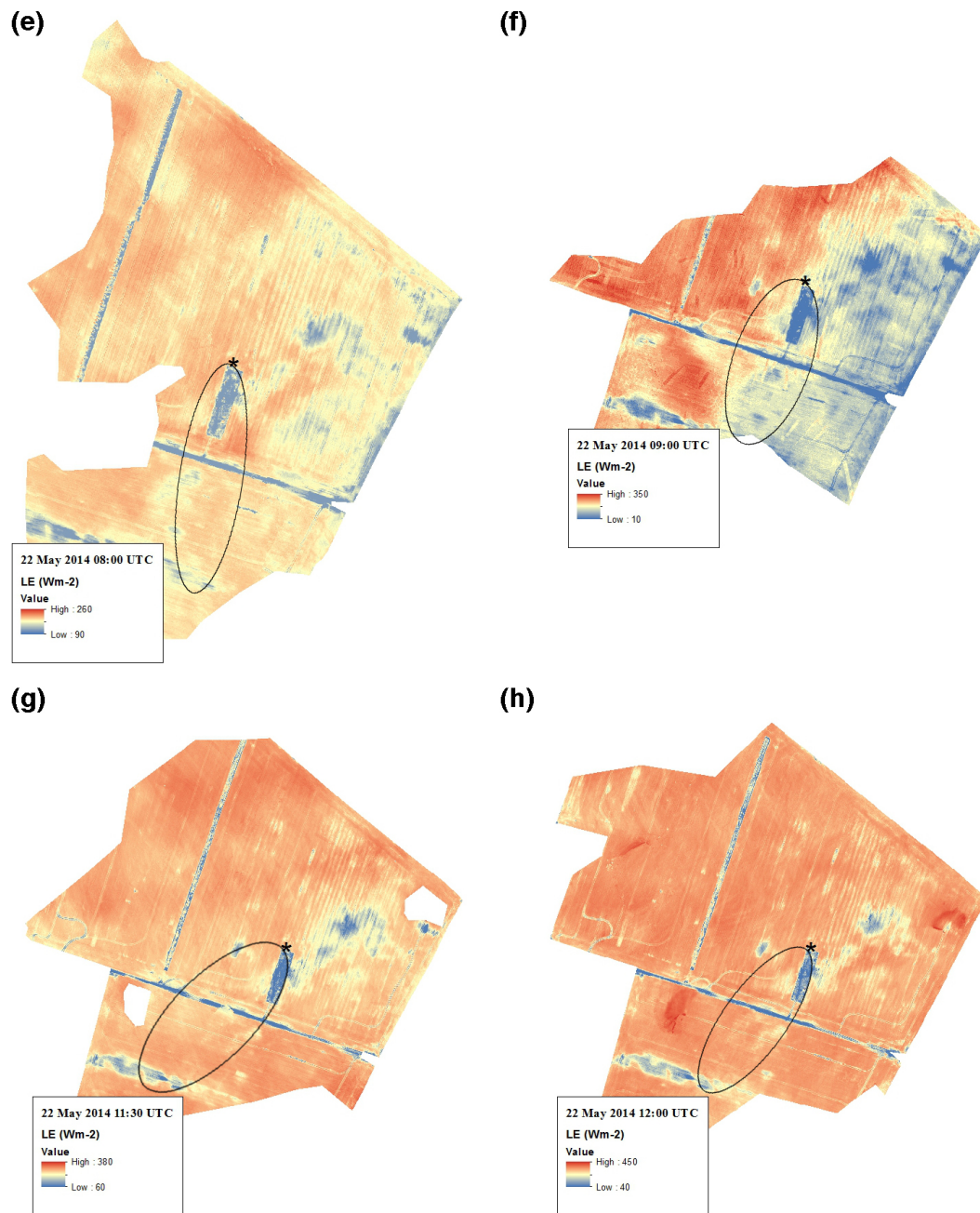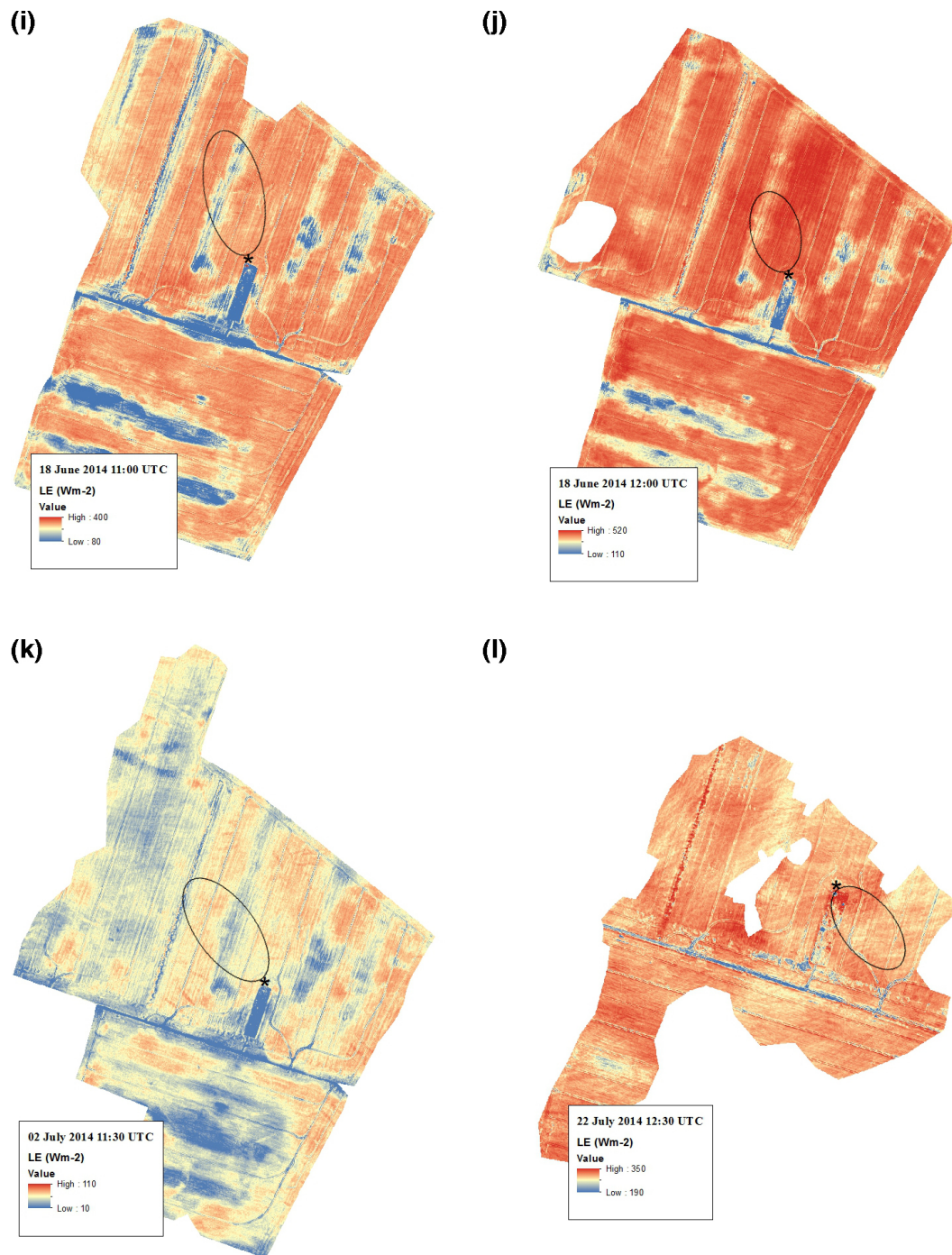
Appendix B: Evaporation maps

(a)

(b)

(c)

(d)

Figure B1.

(e)

(f)

(g)

(h)

Figure B1.

Figure B1. Evaporation maps from the DTD model. The black star represents the location of eddy flux tower and black circles mark the location of eddy covariance footprint.

References

Allen, R. G., Pereira, L. S., Raes, D., and Smith, M.: Crop evapotranspiration – Guidelines for computing crop water requirements-FAO Irrigation and drainage paper 56, FAO Rome, 1–15, 1998.

Anderson, M. C., Norman, J. M., Diak, G. R., Kustas, W. P., and Mecikalski, J. R.: A two-source time-integrated model for estimating surface fluxes using thermal infrared remote sensing, Remote Sens. Environ., 60, 195–216, doi:10.1016/S0034-4257(96)00215-5, 1997.

Anderson, M. C., Norman, J. M., Mecikalski, J. R., Torn, R. D., Kustas, W. P., and Basara, J. B.: A multiscale remote sensing model for disaggregating regional fluxes to micrometeorological scales, J. Hydrometeorol., 5, 343–363, 2004.

Anderson, M. C., Kustas, W. P., Norman, J. M., Hain, C. R., Mecikalski, J. R., Schultz, L., González-Dugo, M. P., Cammalleri, C., d'Urso, G., Pimstein, A., and Gao, F.: Mapping daily evapotranspiration at field to continental scales using geostationary and polar orbiting satellite imagery, Hydrol. Earth Syst. Sci., 15, 223–239, doi:10.5194/hess-15-223-2011, 2011.

Boulet, G., Olioso, A., Ceschia, E., Marloie, O., Coudert, B., Rivalland, V., Chirouze, J., and Chehbouni, G.: An empirical expression to relate aerodynamic and surface temperatures for use within single-source energy balance models, Agr. Forest Meteorol., 161, 148–155, doi:10.1016/j.agrformet.2012.03.008, 2012.

Brutsaert, W.: On a derivable formula for long-wave radiation from clear skies, Water Resour. Res., 11, 742–744, doi:10.1029/WR011i005p00742, 1975.

Brutsaert, W.: Evaporation Into the Atmosphere: Theory, History, and Applications, Kluwer Acad., Norwell, Mass., 299 pp., 1982.

Brutsaert, W.: Hydrology: An Introduction, Cambridge University Press, 2005.

Cappelen, J.: Danmarks klima 2014 – with English Summary, DMI Tech. Rep. 15-01, Danish Meteorol. Inst., Copenhagen, 2015.

Colaizzi, P. D., Kustas, W. P., Anderson, M. C., Agam, N., Tolk, J. A., Evett, S. R., Howell, T. A., Gowda, P. H., and O'Shaughnessy, S. A.: Two-source energy balance model estimates of evapotranspiration using component and composite surface temperatures, Adv. Water Resour., 50, 134–151, doi:10.1016/j.advwatres.2012.06.004, 2012.

Detto, M., Montaldo, N., Albertson, J. D., Mancini, M., and Katul, G.: Soil moisture and vegetation controls on evapotranspiration in a heterogeneous Mediterranean ecosystem on Sardinia, Italy,

Water Resour. Res., 42, W08419, doi:10.1029/2005WR004693, 2006.

Díaz-Varela, R. A., de la Rosa, R., León, L., and Zarco-Tejada, P. J.: High-Resolution Airborne UAV Imagery to Assess Olive Tree Crown Parameters Using 3D Photo Reconstruction: Application in Breeding Trials, Remote Sens., 7, 4213–4232, doi:10.3390/rs70404213, 2015.

Foken, T.: The Energy Balance Closure Problem: An Overview, Ecol. Appl., 18, 1351–1367, 2008.

Foken, T., Aubinet, M., Finnigan, J. J., Leclerc, M. Y., Mauder, M., and Paw U, K. T.: Results Of A Panel Discussion About The Energy Balance Closure Correction For Trace Gases, B. Am. Meteorol. Soc., 92, ES13–ES18, doi:10.1175/2011BAMS3130.1, 2011.

Fratini, G. and Mauder, M.: Towards a consistent eddy-covariance processing: an intercomparison of EddyPro and TK3, Atmos. Meas. Tech., 7, 2273–2281, doi:10.5194/amt-7-2273-2014, 2014.

Gentine, P., Entekhabi, D., and Heusinkveld, B.: Systematic errors in ground heat flux estimation and their correction, Water Resour. Res., 48, W09541, doi:10.1029/2010WR010203, 2012.

Gonzalez-Dugo, V., Goldhamer, D., Zarco-Tejada, P. J., and Fereres, E.: Improving the precision of irrigation in a pistachio farm using an unmanned airborne thermal system, Irrig. Sci., 33, 43–52, doi:10.1007/s00271-014-0447-z, 2014.

Guzinski, R., Anderson, M. C., Kustas, W. P., Nieto, H., and Sandholt, I.: Using a thermal-based two source energy balance model with time-differencing to estimate surface energy fluxes with day–night MODIS observations, Hydrol. Earth Syst. Sci., 17, 2809–2825, doi:10.5194/hess-17-2809-2013, 2013.

Guzinski, R., Nieto, H., Jensen, R., and Mendiguren, G.: Remotely sensed land-surface energy fluxes at sub-field scale in heterogeneous agricultural landscape and coniferous plantation, Biogeosciences, 11, 5021–5046, doi:10.5194/bg-11-5021-2014, 2014.

Guzinski, R., Nieto, H., Stisen, S., and Fensholt, R.: Intercomparison of energy balance and hydrological models for land surface energy flux estimation over a whole river catchment, Hydrol. Earth Syst. Sci., 19, 2017–2036, doi:10.5194/hess-19-2017-2015, 2015.

Harwin, S. and Lucieer, A.: Assessing the Accuracy of Georeferenced Point Clouds Produced via Multi-View Stereopsis from Unmanned Aerial Vehicle (UAV) Imagery, Remote Sens., 4, 1573–1599, doi:10.3390/rs4061573, 2012.

Herrero, J. and Polo, M. J.: Parameterization of atmospheric longwave emissivity in a mountainous site for all sky conditions, Hydrol. Earth Syst. Sci., 16, 3139–3147, doi:10.5194/hess-16-3139-2012, 2012.

Houborg, R., Anderson, M., Gao, F., Schull, M., and Cammalleri, C.: Monitoring water and carbon fluxes at fine spatial scales using HyspIRI-like measurements, 2012 IEEE International Geoscience and Remote Sensing Symposium (IGARSS), Munich, 7302–7305, 2012.

Hunt Jr., E. R., Cavigelli, M., Daughtry, C. S., Mcmurtrey III, J. E., and Walthall, C. L.: Evaluation of digital photography from model aircraft for remote sensing of crop biomass and nitrogen status, Precis. Agric., 6, 359–378, 2005.

Jansen, J. H. A. M., Stive, P. M., Van De Giesen, N. C., Tyler, S. W., Steele-Dunne, S. C., and Williamson, L.: Estimating soil heat flux using Distributed Temperature Sensing, IAHS Publ. 343, in:

GRACE, Remote Sensing and Ground-based Methods in Multi-Scale Hydrology, Proceedings of Symposium J-H01 held during IUGG2011 in July 2011 in Melbourne, Australia, 140–144, 2011.

Kalma, J. D., McVicar, T. R., and McCabe, M. F.: Estimating Land Surface Evaporation: A Review of Methods Using Remotely Sensed Surface Temperature Data, Surv. Geophys., 29, 421–469, doi:10.1007/s10712-008-9037-z, 2008.

Kustas, W. P. and Norman, J. M.: Use of remote sensing for evapotranspiration monitoring over land surfaces, Hydrolog. Sci. J., 41, 495–516, doi:10.1080/02626669609491522, 1996.

Kustas, W. P., Prueger, J. H., and Hipps, L. E.: Impact of using different time-averaged inputs for estimating sensible heat flux of riparian vegetation using radiometric surface temperature, J. Appl. Meteorol., 41, 319–332, 2002.

Liebethal, C. and Foken, T.: Evaluation of six parameterization approaches for the ground heat flux, Theor. Appl. Climatol., 88, 43–56, doi:10.1007/s00704-005-0234-0, 2007.

Lucieer, A., Malenovský, Z., Veness, T., and Wallace, L.: HyperUAS – Imaging Spectroscopy from a Multirotor Unmanned Aircraft System, J. Field Robot., 31, 571–590, doi:10.1002/rob.21508, 2014.

Mauder, M. and Foken, T.: Impact of post-field data processing on eddy covariance flux estimates and energy balance closure, Meteorol. Z., 15, 597–609, doi:10.1127/0941-2948/2006/0167, 2006.

Moncrieff, J., Clement, R., Finnigan, J., and Meyers, T.: Averaging, detrending, and filtering of eddy covariance time series, in: Handbook of micrometeorology, Springer, 7–31, available at: http://link.springer.com/chapter/10.1007/1-4020-2265-4_2 (last access: 3 June 2015), 2005.

Moncrieff, J. B., Massheder, J. M., de Bruin, H., Elbers, J. A., Friborg, T., and Heusinkveld, B.: A system to measure surface fluxes of momentum, sensible heat, water vapour and carbon dioxide, J. Hydrol., 188–189, 589–611, doi:10.1016/S0022-1694(96)03194-0, 1997.

Monteith, J. L.: Evaporation and environment, in: Symp. Soc. Exp. Biol, vol. 19, p. 4, available at: http://www.unc.edu/courses/2007fall/geog/801/001/www/ET/Monteith65.pdf (last access: 17 June 2015), 1965.

Norman, J. M., Kustas, W. P., and Humes, K. S.: Source approach for estimating soil and vegetation energy fluxes in observations of directional radiometric surface temperature, Agr. Forest Meteorol., 77, 263–293, doi:10.1016/0168-1923(95)02265-Y, 1995.

Norman, J. M., Kustas, W. P., Prueger, J. H., and Diak, G. R.: Surface flux estimation using radiometric temperature: A dual-temperature-difference method to minimize measurement errors, Water Resour. Res., 36, 2263–2274, doi:10.1029/2000WR900033, 2000.

Norman, J. M., Anderson, M. C., Kustas, W. P., French, A. N., Mecikalski, J., Torn, R., Diak, G. R., Schmugge, T. J., and Tanner, B. C. W.: Remote sensing of surface energy fluxes at 101-m pixel resolutions, Water Resour. Res., 39, 1221, doi:10.1029/2002WR001775, 2003.

Papale, D., Reichstein, M., Aubinet, M., Canfora, E., Bernhofer, C., Kutsch, W., Longdoz, B., Rambal, S., Valentini, R., Vesala, T., and Yakir, D.: Towards a standardized processing of Net Ecosystem Exchange measured with eddy covariance technique: algorithms and uncertainty estimation, Biogeosciences, 3, 571–583, doi:10.5194/bg-3-571-2006, 2006.

Priestley, C. H. B. and Taylor, R. J.: On the Assessment of Surface Heat Flux and Evaporation Using Large-Scale Parameters, Mon. Weather Rev., 100, 81–92, doi:10.1175/1520-0493(1972)100<0081:OTAOSH>2.3.CO;2, 1972.

Ringgaard, R., Herbst, M., Friborg, T., Schelde, K., Thomsen, A. G., and Soegaard, H.: Energy Fluxes above Three Disparate Surfaces in a Temperate Mesoscale Coastal Catchment, Vadose Zone J., 10, 54, doi:10.2136/vzj2009.0181, 2011.

Santanello, J. A. and Friedl, M. A.: Diurnal Covariation in Soil Heat Flux and Net Radiation, J. Appl. Meteorol., 42, 851–862, 2003.

Shuttleworth, W. J. and Wallace, J. S.: Evaporation from sparse crops-an energy combination theory, Q. J. Roy. Meteorol. Soc., 111, 839–855, 1985.

Stisen, S., Sandholt, I., Nørgaard, A., Fensholt, R., and Jensen, K. H.: Combining the triangle method with thermal inertia to estimate regional evapotranspiration – Applied to MSG-SEVIRI data in the Senegal River basin, Remote Sens. Environ., 112, 1242–1255, doi:10.1016/j.rse.2007.08.013, 2008.

Swain, K. C., Thomson, S. J., and Jayasuriya, H. P.: Adoption of an unmanned helicopter for low-altitude remote sensing to estimate yield and total biomass of a rice crop, T. ASAE, 53, 21–27, 2010.

Turner, D., Lucieer, A., and Watson, C.: An Automated Technique for Generating Georectified Mosaics from Ultra-High Resolution Unmanned Aerial Vehicle (UAV) Imagery, Based on Structure from Motion (SfM) Point Clouds, Remote Sens., 4, 1392–1410, doi:10.3390/rs4051392, 2012.

Wallace, L., Lucieer, A., Watson, C., and Turner, D.: Development of a UAV-LiDAR System with Application to Forest Inventory, Remote Sens., 4, 1519–1543, doi:10.3390/rs4061519, 2012.

Webb, E. K., Pearman, G. I., and Leuning, R.: Correction of flux measurements for density effects due to heat and water vapour transfer, Q. J. Roy. Meteorol. Soc., 106, 85–100, doi:10.1002/qj.49710644707, 1980.

Zarco-Tejada, P. J., González-Dugo, V., Williams, L. E., Suárez, L., Berni, J. A. J., Goldhamer, D., and Fereres, E.: A PRI-based water stress index combining structural and chlorophyll effects: Assessment using diurnal narrow-band airborne imagery and the CWSI thermal index, Remote Sens. Environ., 138, 38–50, doi:10.1016/j.rse.2013.07.024, 2013.

Zarco-Tejada, P. J., Diaz-Varela, R., Angileri, V., and Loudjani, P.: Tree height quantification using very high resolution imagery acquired from an unmanned aerial vehicle (UAV) and automatic 3D photo-reconstruction methods, Eur. J. Agron., 55, 89–99, doi:10.1016/j.eja.2014.01.004, 2014.